



Molecular dynamics simulations of amorphous Ni–P alloy formation by rapid quenching and atomic deposition

Ralf Brüning¹, Delilah A Brown¹, Holger Bera² and Noël Jakse³

¹ Physics Department, Mount Allison University, Sackville, New Brunswick, E4L 1E6, Canada

² Atotech Deutschland GmbH, Erasmusstrasse 20, 10553 Berlin, Germany

³ Univ. Grenoble Alpes, CNRS, Grenoble INP, SIMaP, F-38000, Grenoble, France

E-mail: rbruening@mta.ca (Ralf Brüning)

Received 28 October 2019, revised 28 November 2019

Accepted for publication 9 December 2019

Published 9 January 2020



Abstract

A combined experimental and simulation study is carried out to compare the properties of amorphous $\text{Ni}_{100-x}\text{P}_x$ alloys obtained by electroless deposition and rapid melt-quenching. The onset of crystallization of experimental electroless deposited amorphous films is measured by differential scanning calorimetry experiments. Classical molecular dynamics simulations using Embedded Atom Model-based interactions are performed to obtain glassy Ni–P by melt-quenching the liquid with various quenching rates, as well as *via* low-energy chemical deposition to mimic experimental electroless deposition. It is shown that the deposited amorphous and glassy states display similar short-range order. The amorphous deposit corresponds to a glassy state obtained with a cooling rate of 10^9 K s^{-1} , indicating that deposition yields generally more relaxed amorphous structures. The appearance of phosphorus-enriched surface on the simulated deposited thin film, comparable to experimental observations, is discussed.

Keywords: amorphous metals, Ni–P alloys, thin films, molecular dynamics, electroless deposition, differential scanning calorimetry

(Some figures may appear in colour only in the online journal)

1. Introduction

The report of first metallic glass (MG) [1], made by splat quenching with high cooling rates from the liquid phase, has triggered fundamental questions regarding the similarities and differences of their short-range order with respect to amorphous phases that have been earlier obtained by electrodeposition [2], vapour deposition and other techniques [3, 4]. Early structural models for MGs, such as the dense random hard sphere packing, proposed in the same period by Bernal [5] to describe the local structure of monatomic liquids, or the stereochemical model [6], mapping the short-range order of an alloy on its crystalline counterpart, are known to fail to detect more complex situations such as the competition between local orders [7, 8] or the extension of the local order to the medium-range order [9]. Based on more recent studies by

ab initio and classical molecular dynamics (MD) simulations, metallic liquids display a significant degree of five-fold symmetry (FFS) incompatible with the translational symmetry of the crystal [7, 10–12], as already hypothesized by Frank in the fifties [13]. The FFS, its possible extension to the medium-range order [10, 14], and pentagonal decorated surfaces [15] may hinder crystallization and favour formation of glassy or amorphous phases.

In order to tackle the issue of the structural ordering in glassy and amorphous metals, we consider the $\text{Ni}_{100-x}\text{P}_x$ alloys with $x \approx 20$. Ni–P compounds are interesting for the surface finishing of industrial materials due to their excellent microhardness, corrosion resistance, electrocatalytic activity for hydrogen evolution and special paramagnetic characteristics. Amorphous phases can be prepared by electroless deposition [16], electrodeposition [17, 18] or rapid quenching of

the melt [19, 20]. In electrodeposition, Ni ions are reduced on a substrate acting as the cathode in a plating cell, while in electroless deposition, the Ni ions are reduced on the substrate surface by an autocatalytic reaction with hypophosphite ions. In order to obtain fully amorphous Ni–P samples by rapid quenching, cooling rates on the order of 10^6 K s^{-1} are needed, and we will restrict the use of the term glass to alloys obtained by quenching. The corrosion resistance of electroless Ni–P alloys has been attributed to the formation of a phosphorus-enriched, oxide-free surface layer ($x \leq 50$, thickness below a few Å) [16]. However, the direct comparison of the structural properties coming from the two experimental processes is not obvious and requires an analysis at the atomic level.

MD simulations are a powerful tool to analyze processes of growth of amorphous films and resulting structural properties at the atomic scale. Various types of atomic and nano-structure deposition have been simulated by this method [21]. Most simulations use high particle energies that are appropriate for sputtering, and the dependence on energy has been considered [22]. Simulations of Cu on Cu single crystal deposition with low (sub-thermal) particle energies have been carried out to reproduce conditions relevant for electroless or galvanic plating, and to contrast these low-energy processes with high particle velocity deposition [23]. When both low substrate temperature and low particle energies are employed, one observes rough, faceted plating, reproducing the structure spongy deposits that are obtained with additive-free electroless copper plating baths. Both high particle energy and high substrate temperature promote smooth plating surfaces. However, on a (100) substrate surface higher temperature is more efficient in obtaining a smooth deposit, whereas on a (111) surface higher particle energy is more efficient leveling the deposit surface. These simulation results show that low (thermal or sub-thermal) particle energies are important for MD modelling electroless plating. Therefore, this low-energy deposition process is adopted here to obtain an approximation of the electroless deposition of Ni–P alloys. To our knowledge, formation of amorphous Ni–P alloys by deposition using MD simulations has not yet been reported in the literature.

The present work aims at comparing the two paths of reaching an amorphous state by means of a combined experimental and simulation approach. Differential scanning calorimetry (DSC) is used to locate the glass transition temperature of the electroless amorphous deposit. Molecular dynamics simulations using a semi-empirical potential [24] based on the embedded atom model (EAM) [25–27] are performed: firstly *via* quenching a melt from the liquid state to the glass, which is routinely done [28], and secondly *via* low-energy chemical deposition to mimic experimental electroless deposition. Simulations of melt-quenching yield structural and thermodynamic properties, as well as the glass transition temperatures, that depend on the rate at which the melt is cooled to the glass state [29]. Therefore, glassy states were produced by cooling the melt at three different cooling rates ranging from 10^{13} to 10^{11} K s^{-1} . The structural properties are analyzed through the pair-correlation functions as well as common neighbour analysis (CNA) [30]. The amorphous deposit and glassy states share

common features regarding the short-range order. Based on the evolution of properties as a function of cooling rate from our MD simulations, the deposited amorphous alloy corresponds to a glassy state obtained with a cooling rate of 10^9 K s^{-1} , indicating that deposition is, for a given time scale, more efficient in preparing a relaxed amorphous Ni–P state than quenching. Moreover, a phosphorus-enriched surface appears on the deposited thin film, in accordance with experimental data. The features and implications of this layer are discussed.

2. Technical background

2.1. Simulation method

Classical molecular dynamics simulations were performed using interactions constructed within the framework of the Embedded-Atom Model [25–27]. The potential energy functional for N atoms can be expressed as

$$E = \sum_{i=1}^N \left[F_i(\rho_i) + \frac{1}{2} \sum_{j \neq i=1}^N \Phi_{ij}(r_{ij}) \right], \quad (1)$$

where $F_i(\rho_i)$ is the embedding energy function depending on the background electronic density ρ_i , and $\Phi_{ij}(r_{ij})$ represents a pair potential depending on interatomic distance r_{ij} between atoms i and j . The parameters of equation (1) specific to Ni–P alloys were determined by Sheng *et al* [24]. These were treated as mathematical entities and allowed to vary to produce best matches between EAM and first-principles calculations.

For the purpose of studying the properties of amorphous deposits and melt-quenched glasses, we have carried out classical MD simulations with the EAM potential using the LAMMPS code [31]. The equations of motion were solved numerically with the Verlet algorithm in the velocity form [32, 33] using a 1 fs time step.

For melt-quenching, all MD simulations were performed in the isobaric-isothermal ensemble (constant temperature, pressure and number of particles) with ambient pressure. In a first stage, a $\text{Ni}_{80}\text{P}_{20}$ alloy is represented by $N = 163\,840$ atoms (131\,072 Ni and 32\,768 P) in a cubic simulation box with an edge length of approximately 122 Å, subject to the standard periodic boundary conditions in the three directions of space. It is equilibrated for 100 ps at a temperature $T = 2000 \text{ K}$ from an initial configuration with random atomic positions. In a second stage, the system is cooled down to 0 K with a cooling rate of 10^{11} K s^{-1} . During this process, thermodynamic properties are calculated and recorded every 10 time steps. For $T = 300 \text{ K}$, we took the corresponding configuration and brought the system to equilibrium for a period of 10 ns at constant temperature and pressure. Structural properties were subsequently measured during 1 ns. This procedure is repeated with cooling rates of 10^{12} K s^{-1} and 10^{13} K s^{-1} .

For the MD simulations of deposition, an amorphous 18 Å thick substrate with 15\,332 Ni and 3\,809 P atoms was extracted from the melt-quenched glass. The latter was initially relaxed after release of the periodic boundary condition in the z direction using a standard conjugate gradient minimization method. The MD simulation is then conducted for

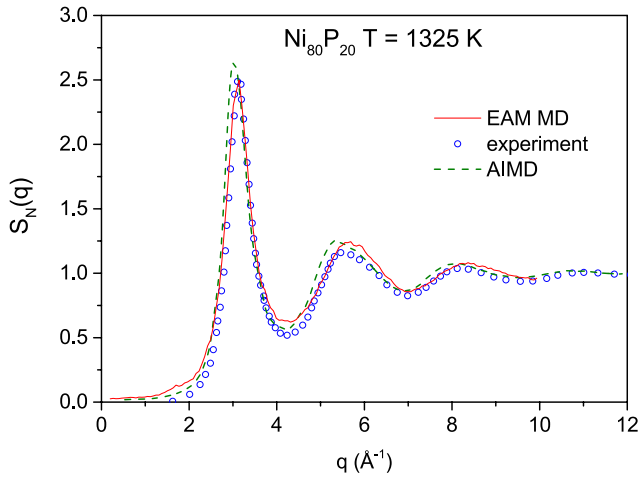


Figure 1. Total structure factor from Neutron diffraction of $\text{Ni}_{80}\text{P}_{20}$ alloy in the liquid state at $T = 1325$ K. Classical MD results are compared to AIMD results and experimental data of Dahlborg *et al* [40].

30 ns time in the canonical ensemble (constant temperature, volume and number of particles), maintaining the substrate at $T = 300$ K. During this isotherm, atoms are deposited on the surface at a rate of $2.5 \text{ atoms ps}^{-1}$ starting at the height of 5 Å with an initial velocity of 1.5 Å ps^{-1} (150 m s^{-1} , i.e. $\approx 5 \text{ meV}$ depending on the atom type). This process is intended to mimic low-energy electroless deposition. It differs from e.g. sputtering, where particles are deposited with energies of several electron volts. In order to investigate the effect of the substrate, the deposition is repeated on a (1 1 1) fcc-Cu crystal surface. An EAM potential for Cu–Ni alloys has been used [34] to describe interactions between Cu and Ni atoms and combined to the Ni–P EAM potential using the hybrid mode of LAMMPS.

Ab initio molecular dynamics (AIMD) were used for testing the reliability of the EAM potential in describing the liquid structure of $\text{Ni}_{80}\text{P}_{20}$ alloy in the liquid state at $T = 1325$ K. The AIMD simulation has been carried out within the framework of the density-functional theory (DFT) using the Vienna *ab initio* simulation package [35, 36] with a plane-wave basis set. The energy cutoff had the standard value of 1077.67 eV . The projected augmented-wave method was used to describe the electron-ion interaction [37, 38] and the exchange-correlation energy was taken from the generalized gradient approximation [39]. The dynamics was carried out in the canonical ensemble, and Newton’s equations of motion were integrated using Verlet’s algorithm in the velocity form with a 1.0 fs time step. A cubic simulation box with periodic boundary conditions containing 135 atoms (108 Ni and 27 P) was used, and only the Γ -point sampling is considered to sample the supercell Brillouin zone. The simulation, starting from an initial configuration with random positions, was equilibrated at $T = 2000 \text{ K}$ for 10 ps before cooling to the target temperature at 10^{12} K s^{-1} . After a new equilibration for 10 ps the run was continued for 30 ps to calculate the structural properties.

2.2. Experimental procedure

A $7.7 \mu\text{m}$ thick $\text{Ni}_{81}\text{P}_{19}$ film was prepared by electroless plating for 1.0 h from an acidic bath at $\text{pH} = 4.9$ and 85°C on a stainless steel substrate. In order to initiate the electroless reaction a battery was used for a few seconds to avoid incorporation of impurities which can come from a substrate activation procedure. Subsequently, autocatalytic deposition occurs. After plating, the deposit was peeled from the substrate to obtain a free-standing film. X-ray diffraction measurements ($\text{Cu-K}\alpha$ radiation, graphite monochromator and analyzer crystals), carried out both in reflection and transmission mode, show no sign of crystallization. X-ray fluorescence shows that the phosphorus concentration at the base of the film is $1.8 \pm 1.5 \%$ higher than on top of the film. Differential scanning calorimetry measurements were carried out with a Perkin–Elmer DSC 7.

3. Results and discussion

In a first stage, the reliability of the EAM potential is tested against existing experimental data and *ab initio* calculations in the liquid and amorphous states. In figure 1 the total neutron scattering structure factor obtained by MD and AIMD in the liquid state at $T = 1325 \text{ K}$ is compared with experimental data of Dahlborg *et al* [40]. Both $S_N(q)$ simulation curves have been calculated using the ISAACS software [41]. An overall good agreement is seen between experimental data and both MD and AIMD results. More specifically, the first peak position, its height and the low- q behavior are reproduced showing the reliability of the EAM potential in describing the structure at the local and intermediate scales.

A more detailed assessment of the local structure can be made through the partial pair-correlation functions, $g(r_{ij})$. Figure 2(a) shows a comparison of the $g(r_{ij})$ s between the MD and AIMD results in the liquid state at $T = 1325 \text{ K}$. Agreement is found for the three partial pair-correlation functions, indicating that the chemical ordering is well reproduced as compared to *ab initio* calculations showing a strong Ni–P affinity and the absence of P–P first neighbours. Nevertheless, the EAM potential gives a less pronounced Ni–P affinity and slightly shorter Ni–Ni distances with respect to the AIMD results.

In figure 2(b), the pair-correlation functions $G_{ij}(r) = r[g_{ij}(r) - 1]$ are then compared with the experimental data [20] for the glass at $T = 300 \text{ K}$. The MD curves obtained from the melt-quenching with the lowest cooling rate, i.e. 10^{11} K s^{-1} , agree with the three measured partials. The structural features of the glass are better defined than those of the liquid state. The absence of P–P first neighbours seen in the liquid persists in the glassy state, and the second peak of the Ni–Ni partial splits with possible pronounced FFS ordering around Ni atoms.

A snapshot of the bulk glassy state at $T = 300 \text{ K}$ out of the melt-quenching MD simulation with the cooling rate of 10^{11} K s^{-1} has been drawn in figure 3(a) using the OVITO

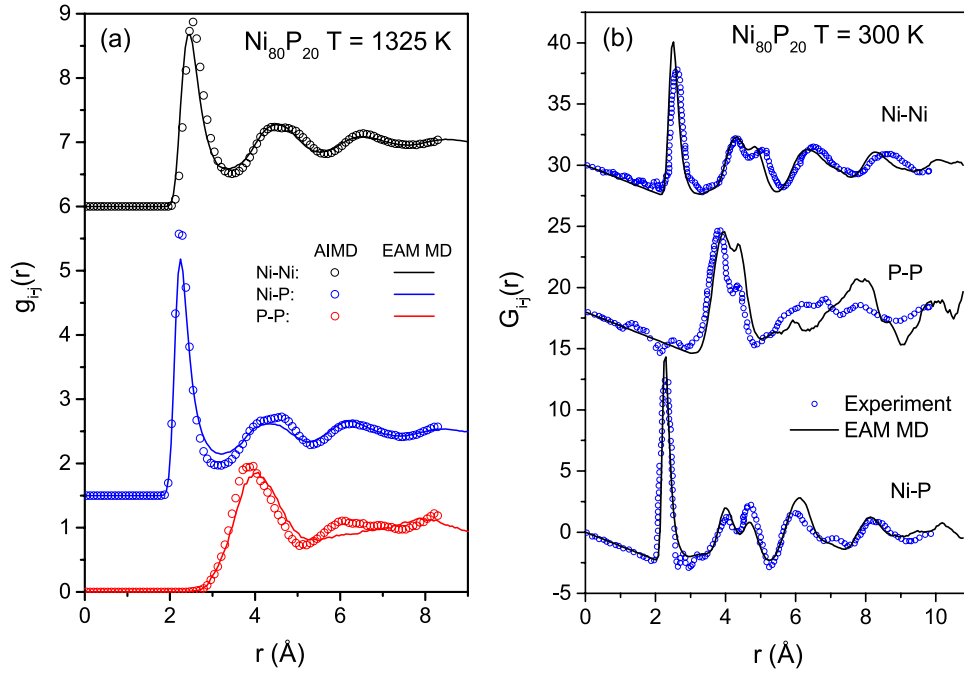


Figure 2. (a) Partial pair-correlation functions of $\text{Ni}_{80}\text{P}_{20}$ alloy in the liquid state at $T = 1325$ K. Classical MD results with the EAM potential are compared to AIMD results for the liquid state at $T = 1325$ K. For visual purpose, the Ni-P and Ni-Ni curves are shifted up by 1.5 and 6, respectively. (b) Partial pair-correlation functions $G_{ij}(r) = r(g_{ij}(r) - 1)$ of $\text{Ni}_{80}\text{P}_{20}$ alloy in the glassy state at $T = 300$ K obtained from the melt-quenching technique and compared to the experimental data of Lamparter *et al* [20].

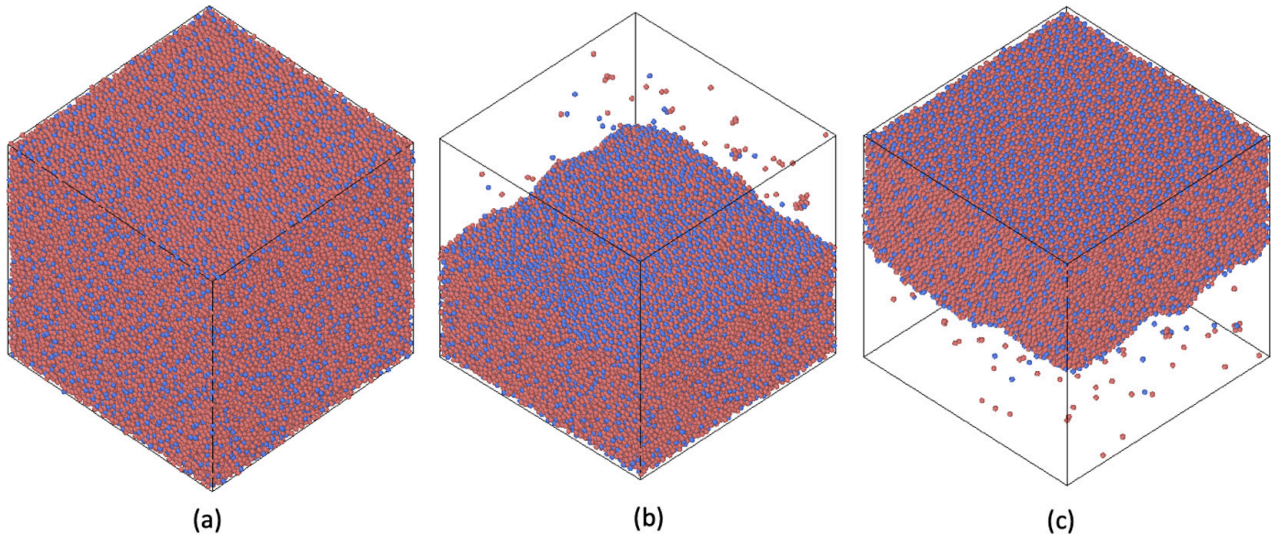


Figure 3. Images of the simulation cells, with Ni and P atoms shown in red and blue, respectively: (a) Snapshot of bulk glass quenched at 10^{11} K s^{-1} , (b) top side and (c) bottom side of the simulated electroless deposit. The bulk glass has periodic boundary conditions in x , y and z . The deposit has periodic boundary conditions along x and y and free z -surfaces with edge lengths of $\approx 122 \text{ Å}$.

visualization tool [42], which shows an homogeneous situation. As described in the preceding Section, a 18 Å thick slab has been taken from such a configuration to serve as an amorphous substrate for the deposition. Figures 3(b) and (c) show the resulting structure after the atom-by-atom deposition process. The ratio of the MD simulation quench rates (10^{11} – 10^{13} K s^{-1}) to typical laboratory melt-spinning quench rates, 10^6 K s^{-1} , is about 10^6 . Based on comparable computational effort, the ratio between the simulated deposition rate (1.9 mm s^{-1}) and the laboratory electroless deposition rate (2.1 nm s^{-1}) is the same. Therefore, the simulations of

quenching and deposition reproduce the ratio of the time scales of the corresponding laboratory experiments.

The simulation results in figure 3 reveal two important features: (i) All surfaces that correspond to periodic boundary conditions are indistinguishable in appearance, which suggests that the atomic structures of the deposit and the glass are similar; (ii) phosphorus atoms chemically segregate at the free top and bottom surfaces of the deposit. This chemical segregation at the surface is discussed further below.

In the course of modelling electroless deposition, we found that the use of an amorphous substrate is essential. Initial tests

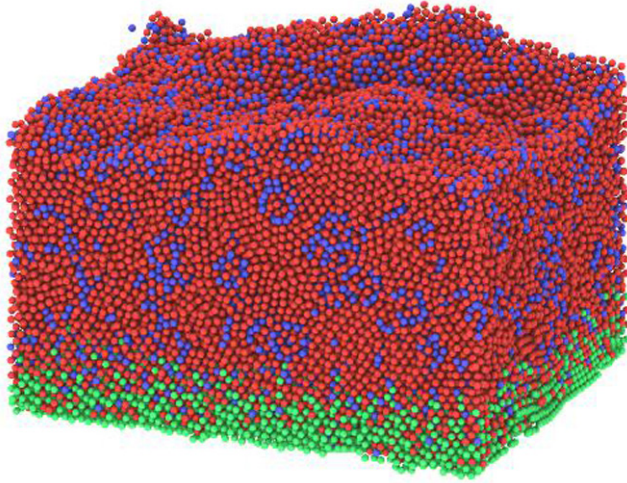


Figure 4. Simulated electroless $\text{Ni}_{80}\text{P}_{20}$ deposit on a Cu (111) single fcc crystal substrate. Ni, P and Cu atoms are shown in red, blue, and green color, respectively.

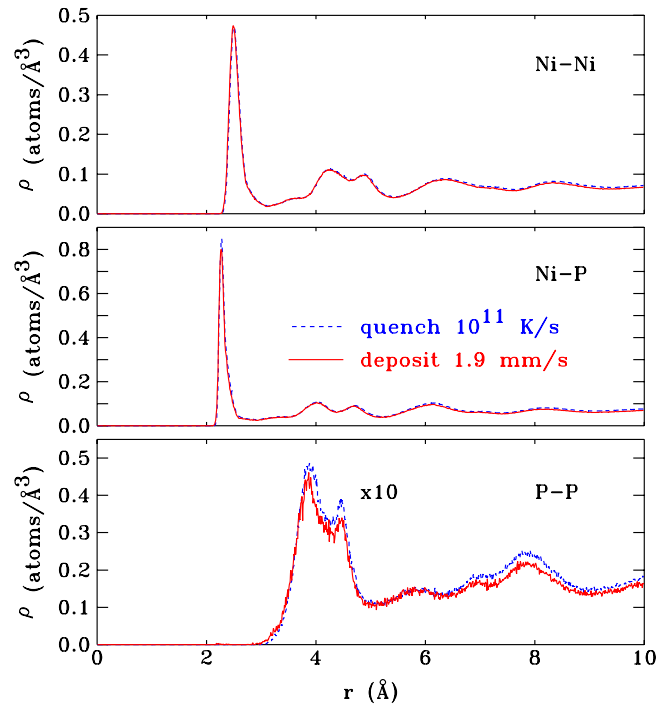


Figure 5. Partial number densities of the inherent structures for the quenched glass (blue dotted line) and the deposit (red solid line). For the deposit, central atoms were restricted to the range $28 \text{ \AA} < z < 45 \text{ \AA}$ to exclude the substrate and surface regions.

with a fcc-Cu substrate yielded a partially crystalline film consisting of fcc-Ni crystallites with the P concentrated in lines at grain boundary triple junctions (figure 4), showing that the atomic configuration at the surface of the substrate is important [15]. Therefore, also for this model of electroless deposition, the composition $\text{Ni}_{80}\text{P}_{20}$ is at the edge of compositions yielding amorphous films.

The similarity of the glass and the bulk of the deposit is confirmed by the partial number densities shown in figure 5. In order to allow a finer comparison, the inherent structures of the simulated configurations were determined by bringing

Table 1. Abundance of pairs from the CNA analysis in the bulk glass and the amorphous deposit around Ni and P atoms. The uncertainties are approximately 1%.

Pairs	Glass		Deposit	
	Ni	P	Ni	P
555	0.221	0.212	0.225	0.213
554	0.239	0.172	0.240	0.177
433	0.222	0.257	0.219	0.248
421	0.102	0.110	0.100	0.103
422	0.052	0.052	0.051	0.048
444	0.027	0.056	0.030	0.060
666	0.047	0.024	0.052	0.028

the system to the local minimum of the potential energy surface to suppress the thermal noise. The largest difference is a higher frequency of the P-P pairs for the quenched structure, due to the reduced phosphorus concentration in the bulk of the deposit caused by the surface segregation. The number of Ni-P pairs in the deposit is reduced accordingly.

We use CNA to make more detailed comparison between the deposit and bulk glass [30]. CNA determines local topologies like fcc, hcp, bcc and icosahedral, as well as more complex polytetrahedral environments. We refer the reader to [43] for a detailed description. The CNA is applied to the inherent structures and identifies pairs around each atom which are classified by sets of three indices. The first index represents the number of near neighbours shared by a pair, the second index states the number of nearest-neighbour bonds among the shared neighbours, and the third index indicates the longest chain of bonded atoms among them. For instance, 421 and 422 bonded pairs are characteristic of close packed structures fcc and hcp, respectively. The occurrence of 444 and 666 pairs, with specific proportions, signals the presence of bcc ordering. The degree of five-fold symmetry is obtained by considering the proportion of 555, 554 and 433 pairs, which represent perfect (555) and distorted FFS based motifs. Table 1 lists the most abundant pairs for the glass and the deposit. Strikingly, the three-dimensional local topology for the glass and deposit are very similar. Both structures display a strong FFS component around both atom types, although the one in P environments is more defective than for Ni. Such a strong FFS is comparable to that for pure liquid Ni [44] and Ni-rich Al-Ni alloys [45], which is an indication that the FFS might be influenced by Ni. The CNA further indicated that significant fcc ordering persists as attested by the presence of about 10% 421 pairs, while the bcc ordering remains always small. Even though a fcc ordering is present in our structure, no pure Ni inclusions could be detected, as was hypothesized recently [40].

The average density characterizes the thermodynamic state of the amorphous structures. For the bulk glasses it depends on the quench rate, as shown in figure 6. Regarding the deposit, we consider its central region with $20 \text{ \AA} < z < 50 \text{ \AA}$, thereby excluding the substrate and the surface regions identified in figure 7. The specific volume in this region at 300 K, $11.107 \pm 0.016 \text{ \AA}^3$, is also shown in figure 6. The specific volume of the bulk liquid decreases upon cooling as shown in

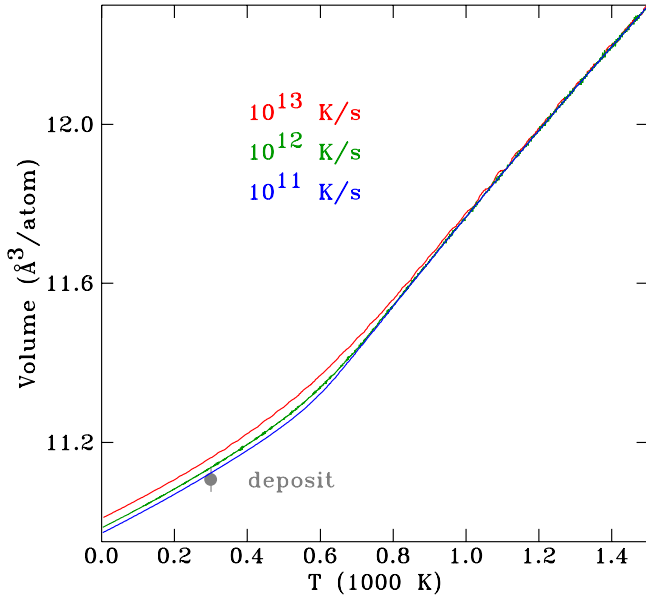


Figure 6. Specific volume of the simulated bulk $\text{Ni}_{80}\text{P}_{20}$ upon cooling at the indicated rates (lines), and of the simulated deposit in the region $20 \text{ Å} < z < 50 \text{ Å}$ at 300 K (point).

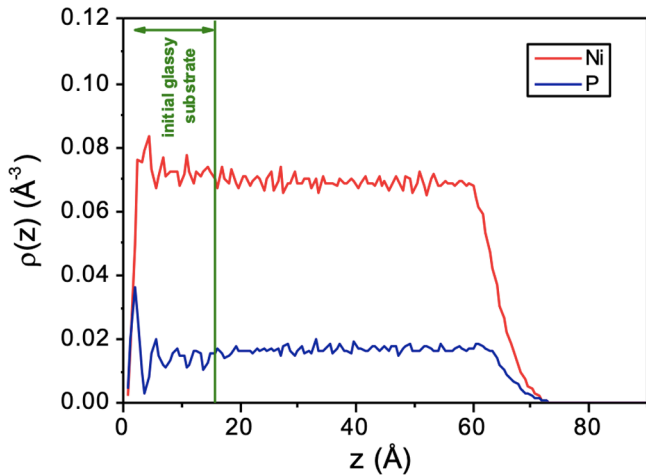


Figure 7. Number densities of deposited Ni and P atoms as a function of distance from the base of the substrate at the end of the deposition.

figure 6. Above 800 K, the volume of the supercooled liquid is independent of the cooling rate. Below 500 K, slower cooling rates yield denser glasses. We see that the deposition yields an amorphous structure that is denser than that of the bulk glass quenched at 10^{11} K s^{-1} . Accordingly, the Ni–Ni and Ni–P pair distributions in figure 5 are shifted to larger radii in the quenched glass relative to the deposit.

When a supercooled liquid is to be cooled below the glass transition temperature, T_g , its structural state becomes frozen. The degree of disorder in glassy and amorphous systems can be described by a fictive temperature, T_f , that corresponds to the glass transition upon cooling [46]. By considering the change in the thermal expansion coefficient in the vicinity of T_g , shown in figure 8, the volume data can be converted to fictive temperatures shown in table 2. The fictive temperatures of the model deposit, 551 K is lower than of the glass

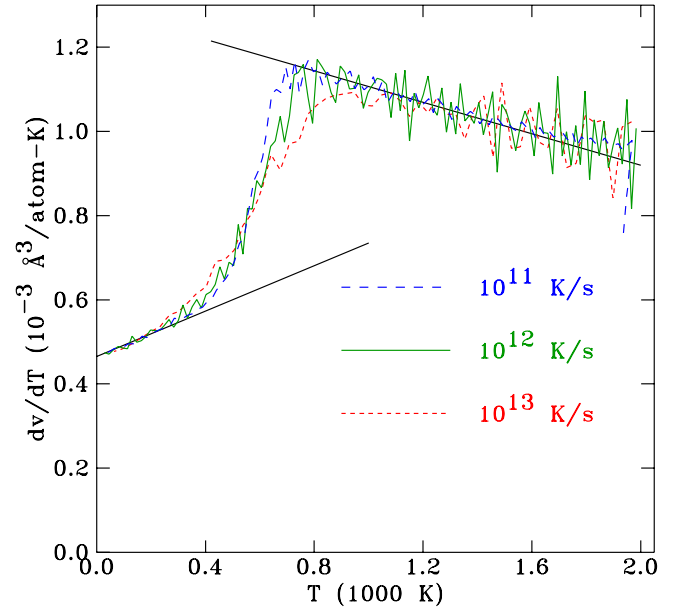


Figure 8. Thermal expansion rate of the simulated bulk liquid upon cooling at the indicated rates. The glass transition becomes narrower and better defined as the cooling rate is reduced. For the estimates of the fictive temperature, the thermal expansion coefficients below and above the glass transition were extrapolated by the straight lines shown in the diagram.

quenched with 10^{11} K s^{-1} (580 K). By extrapolation, the fictive temperature of the deposit is roughly that of a glass quenched at $3 \times 10^9 \text{ K s}^{-1}$. This difference could be the result of the isothermal relaxation of the already-deposited atoms during the remaining deposition time, or it could be a result of fewer constraints on atomic ordering as the deposit is built up atomic layer by atomic layer in the deposition process therefore yielding a denser structure.

Next we consider data obtained with a $7.7 \mu\text{m}$ thick electroless $\text{Ni}_{81}\text{P}_{19}$ film deposited on steel. After plating, the film was peeled from the substrate to obtain a free-standing film. The film is amorphous by transmission and reflection x-ray diffraction measurements (figure 9). Figure 10 shows results from differential calorimetry scans of this deposit upon heating. The onset of crystallization is between 570 and 600 K, depending on the heating rate. Both traces show a small endothermic upturn just before the negative exothermic peak, very similar to a thermogram 17.1% P in [47]. We interpret this endothermic feature as the beginning of the glass transition, with the system crystallizing rather than completing this process. Since this upturn in the heating curve is probably below the normally considered onset of the glass transition, we estimate $T_g \approx 580 \text{ K}$ for the electroless deposit, in agreement with the clearly-observed T_g in $\text{Pd}_{40}\text{Ni}_{40}\text{P}_{20}$ [48]. While the numerical agreement between the computer model and the physical deposit is good, there is a discrepancy because the model rates of about 10^{11} K s^{-1} have to be extrapolated to the experimental laboratory rates ($\sim 1 \text{ K s}^{-1}$), i.e. the glass transition temperature of the model is below that of the physical system.

As mentioned above, figures 3(b) and (c) show how the phosphorus atoms segregate at the free surfaces of the model

Table 2. Fictive temperatures based on specific volume for the simulated quenched glasses and the simulated electroless deposit, as well as an estimate of the glass transition upon heating for the physical electroless deposit.

System	T_f (K)
Model glass, 10^{13} K s^{-1}	650 ± 7
Model glass, 10^{12} K s^{-1}	605 ± 5
Model glass, 10^{11} K s^{-1}	580 ± 5
Model deposit (30 ns)	551 ± 29
Electroless deposit (1 h)	$T_g \approx 580$

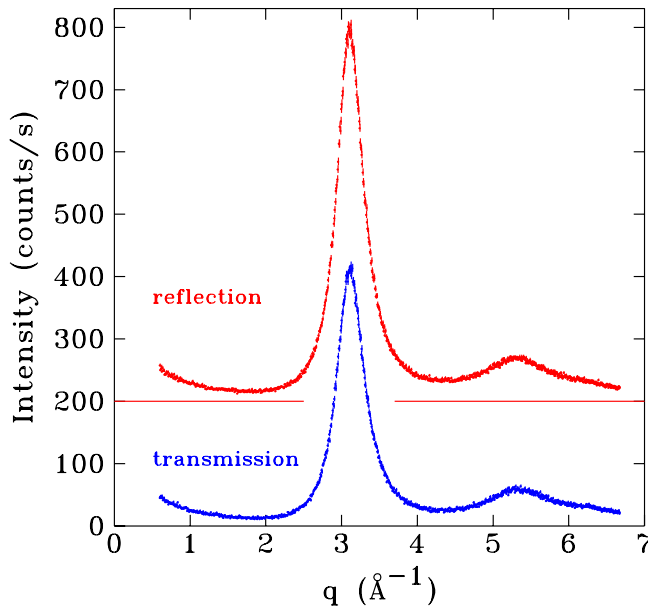


Figure 9. X-ray scattering of the electroless $\text{Ni}_{81}\text{P}_{19}$ deposit as a function of the length of the scattering vector measured in transmission and reflection mode (data shifted up by $200 \text{ counts s}^{-1}$). Error bars correspond to counting statistics. The increase of the signal at small q is mainly due to scattering by ambient air.

structure within a time of 3 ns. Interestingly, the phosphorus atoms do not form a surface layer in figure 4, indicating that for the crystallized system the free energy of P atoms in grain boundary triple junctions is lower than at the surface sites. Figure 7 shows the variations in the densities of nickel and phosphorus atoms. The segregation process at the base of the substrate, at $z = 0$, leads to a layer with about equal numbers of Ni and P atoms. This chemical ordering persists for about two damped oscillations until the bulk densities are reached. The deposition surface is uneven with a z -range from 62 to 72 Å , so that this pattern cannot be observed. Nonetheless, the Ni and P densities converge at high z , showing that also at the deposition surface the Ni–P atomic ratio is also approximately 1:1. This implies that in the model the $\text{Ni}_{80}\text{P}_{20}$ bulk material grows from a layer with an approximate composition $\text{Ni}_{50}\text{P}_{50}$, with a net transport of Ni atoms through this layer. We speculate that, within the modelling, this layer is enabled by the low kinetic energy of the deposited atoms. A simulation with high deposition energies would presumably continuously destroy this layer, so that it would not be observed during deposition.

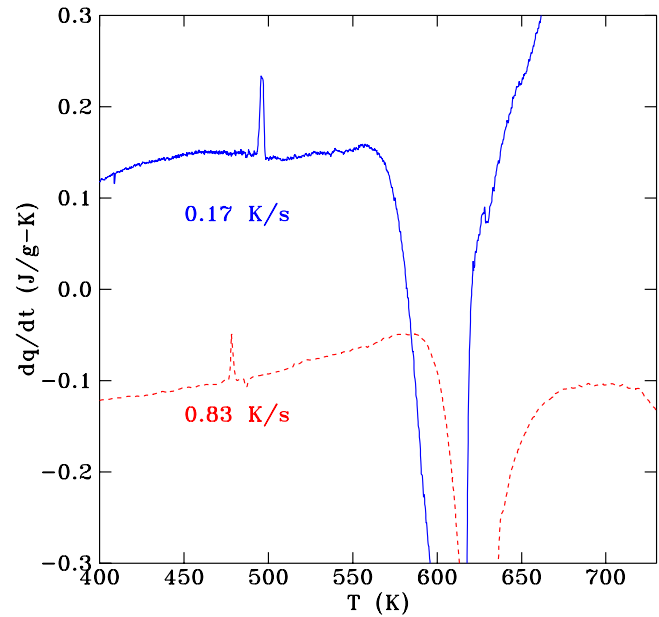


Figure 10. Heatflow of an electroless $\text{Ni}_{81}\text{P}_{19}$ deposit upon heating at two rates. The deposit was peeled from a stainless steel substrate. The crystallization (downward peaks) interrupts the glass transition, the beginning of which is seen as small upwards peaks at 560 K at 0.17 K s^{-1} and 590 K at 0.83 K s^{-1} .

A P-enriched $10 \pm 3 \text{ Å}$ thick surface layer, with about 40% P, has been shown to exist on mechanically polished electroless $\text{Ni}_{82}\text{P}_{18}$ [49], in agreement with the simulation result in figure 7. Because nickel depletes preferentially from the surface, upon corrosion testing the layer grows to $20 \pm 6 \text{ Å}$, and it becomes further enriched in phosphorus (46% P), [49]. Even on the mechanically polished sample there is a layer of nickel phosphate, so that corrosion cannot be excluded from playing a role in forming this layer during the polishing. In any case, the experiment and the simulation show that compositions near $\text{Ni}_{50}\text{P}_{50}$ are thermodynamically stable at the surface. Data from a surface cleaved in vacuum would be needed to see if the spontaneous atomic ordering seen in the simulation does take place. A composition near $\text{Ni}_{50}\text{P}_{50}$ should, however, be considered to be the autocatalytic surface for the electroless plating process.

4. Conclusion

The present work compares the effects of two paths to obtain a Ni–P amorphous state around 20 at% of P. For this purpose, MD simulations of melt-quenching and of low-energy electrochemical deposition were carried out. The results were checked with experimental data from DSC and diffraction measurements. Based on density, the simulated deposit is in a relaxed state relative to simulated quenched glasses, in agreement with the observation that electrodeposited amorphous Ni–P alloys are typically in a thermodynamically relaxed state. While the relaxation states of deposit and glass differ, their local atomic environments are similar in terms of the results of a common neighbour analysis and partial radial distribution functions.

A P-rich surface layer forms spontaneously in about 3 ns, in agreement with experimental observations for mechanically polished electroless samples. However, such a high-P layer does not form on a simulated nanocrystalline material. The glass transition temperature for the MD model is close to the onset of crystallization, and possibly to the glass transition of the physical deposit. This is a strong indication of the reliability of the simulation procedure employed here. Simulations of deposition on amorphous and crystalline substrates show that the substrate choice is important for the plating result.

Acknowledgments

The authors would like to thank Dr. David Fleming, Mount Allison University, for carrying out XRF measurements. We acknowledge the CINES and IDRIS under Project N INP2227/92914, as well as CIMENT/GRICAD for computational resources. This work was performed within the framework of the Centre of Excellence of Multifunctional Architected Materials ‘CEMAM’ ANR-10-LABX-44-01 funded by the ‘Investments for the Future’ program.

ORCID iDs

Ralf Brüning  <https://orcid.org/0000-0002-9030-7860>

Noël Jakse  <https://orcid.org/0000-0002-4031-0965>

References

- [1] Klement W, Willens R H and Duwez P 1960 *Nature* **187** 869
- [2] Brenner A, Couch D E and Williams E K 1950 *J. Res. Natl. Bur. Stand.* **44** 109
- [3] Behrndt K H 1970 *J. Vac. Sci. Technol.* **7** 385
- [4] Daly B P and Barry F J 2003 *Int. Mat. Rev.* **48** 326
- [5] Bernal J D 1960 *Nature* **185** 68
- [6] Gaskell P H 1978 *Nature* **276** 484
- [7] Jakse N and Pasturel A 2003 *Phys. Rev. Lett.* **91** 195501
- [8] Jakse N, Lebacqz O and Pasturel A 2004 *Phys. Rev. Lett.* **93** 207801
- [9] Lan S et al 2019 *Commun. Phys.* **2** 1
- [10] Sheng H W, Luo W K, Alamgir F M, Bai J M and Ma E 2006 *Nature* **439** 419
- [11] Kang J et al 2012 *Phys. Rev. Lett.* **107** 115901
- [12] Hu Y C, Li F X, Li M Z, Bai H Y and Wang W H 2015 *Nat. Commun.* **6** 8310
- [13] Frank F C 1952 *Proc. R. Soc. A* **215** 43
- [14] Lad K N, Jakse N and Pasturel A 2012 *J. Chem. Phys.* **136** 104509
- [15] Pasturel A and Jakse N 2018 *Sci. Rep.* **8** 14314
- [16] Elsener B, Crobu M, Scorciapino M A and Rossi A 2008 *J. Appl. Electrochem.* **38** 1053
- [17] Pittermann U and Ripper S 1985 *Rapidly Quenched Metals* ed S Steeb and H Warlimont (Amsterdam: Elsevier) p 385
- [18] Lelevic A and Walsh F C 2019 *Surf. Coat. Technol.* **369** 198
- [19] Davis L A, Chou C-P, Tanner L E and Ray R 1976 *Scr. Met.* **10** 937
- [20] Lamparter P and Steeb S 1985 *Rapidly Quenched Metals* ed S Steeb and H Warlimont (Amsterdam: Elsevier) p 495
- [21] Braut P and Neyts E C 2015 *Catalysis Today* **256** 3
- [22] Yang Y G, Zhou X W, Johnson R A and Wadley H N G 2001 *Acta Mater.* **49** 3321
- [23] Jakse N and Brüning R (to be published)
- [24] Sheng H W, Ma E and Kramer M J 2012 *JOM* **64** 856
- [25] Daw M S and Baskes M I 1983 *Phys. Rev. Lett.* **50** 1285
- [26] Daw M S and Baskes M I 1984 *Phys. Rev. B* **29** 6443
- [27] Ercolessi F and Adams J B 1994 *Europhys. Lett.* **26** 583
- [28] Royall C P and Williams S R 2015 *Phys. Rep.* **56** 1
- [29] Binder K and Kob W 2005 *Glassy Materials and Disordered Solids* (Singapore: World Scientific) (<https://doi.org/10.1142/5948>)
- [30] Honeycutt J D and Andersen H C 1987 *J. Phys. Chem.* **91** 4950
- [31] Plimpton S J 1995 *J. Comput. Phys.* **117** 1
- [32] Allen M P and Tildesley D J 2017 *Computer Simulation of Liquids* 2nd edn (Oxford: Oxford Science Publication) (<https://doi.org/10.1093/oso/9780198803195.001.0001>)
- [33] Smit B and Frenkel D 2002 *Understanding Molecular Simulations* 2nd edn (New York: Academic) (<https://doi.org/10.1016/B978-0-12-267351-1.X5000-7>)
- [34] Sheng H W, Kramer M J, Cadieu A, Fujita T and Chen M W 2011 *Phys. Rev. B* **83** 134118
- [35] Kresse G and Hafner J 1993 *Phys. Rev. B* **48** 13115
- [36] Kresse G and Hafner J 1994 *Phys. Rev. B* **49** 14251
- [37] Kresse G and Furthmüller J 1996 *Comput. Mat. Sci.* **6** 15
- [38] Kresse G and Joubert D 1999 *Phys. Rev. B* **59** 1758
- [39] Perdew J P, Burke K and Ernzerhof M 1996 *Phys. Rev. Lett.* **77** 3865
- [40] Dahlborg U, Gasser J-G, Cuello G J, Mehraban S, Lavery N and Calvo-Dahlborg M 2018 *J. Non-Cryst. Solids* **500** 359
- [41] Le Roux S and Petkov I 2010 *J. Appl. Cryst.* **43** 181
- [42] Stukowski A 2010 Visualization and analysis of atomistic simulation data with OVITO-the open visualization tool *Modelling Simul. Mater. Sci. Eng.* **18** 015012
- [43] Jakse N and Pasturel A 2006 *Mod. Phys. Lett. B* **20** 655
- [44] Jakse N and Pasturel A 2004 *J. Chem. Phys.* **120** 6124
- [45] Jakse N and Pasturel A 2015 *J. Chem. Phys.* **143** 084504
- [46] Tool A Q 1946 *J. Am. Ceram. Soc.* **29** 240
- [47] Bonino J-P, Bruet-Hotellaz S, Bories C, Pouderoux P and Rousset A 1997 *J. Appl. Electrochem.* **27** 1193
- [48] Jiang J, Saksl K, Nishiyama N and Inoue A 2002 *J. Appl. Phys.* **92** 3651
- [49] Scorciapino M A, Fantauzzi M, Crobu M, Navarra G, Elsener B and Rossi A 2017 *ACS Omega* **2** 7790